Magnetic Resonance in Medicine 59:365–373 (2008)

Compressed Sensing in Dynamic MRI

Urs Gamper, Peter Boesiger, and Sebastian Kozerke*

Recent theoretical advances in the field of compressive sampling—also referred to as compressed sensing (CS)—hold considerable promise for practical applications in MRI, but the fundamental condition of sparsity required in the CS framework is usually not fulfilled in MR images. However, in dynamic imaging, data sparsity can readily be introduced by applying the Fourier transformation along the temporal dimension assuming that only parts of the field-of-view (FOV) change at a high temporal rate while other parts remain stationary or change slowly. The second condition for CS, random sampling, can easily be realized by randomly skipping phase-encoding lines in each dynamic frame. In this work, the feasibility of the CS framework for accelerated dynamic MRI is assessed. Simulated datasets are used to compare the reconstruction results for different reduction factors, noise, and sparsity levels. In vivo cardiac cine data and Fourier-encoded velocity data of the carotid artery are used to test the reconstruction performance relative to *k-t* broad-use linear acquisition speed-up technique (*k-t* BLAST) reconstructions. Given sufficient data sparsity and base signal-to-noise ratio (SNR), CS is demonstrated to result in improved temporal fidelity compared to *k-t* BLAST reconstructions for the example data sets used in this work. Magn Reson Med 59:365–373, 2008. © 2008 Wiley-Liss, Inc.

Key words: compressed sensing; sparsity; dynamic MRI; random sampling; accelerated imaging; undersampling

Conventionally, the data of a dynamic object are acquired frame by frame under the assumption that the motion during the acquisition time for one frame is smaller than the chosen pixel size. Due to the sequential and hence slow acquisition process in MRI, this premise is often violated and leads to a loss in image quality or necessitates the choice of a lower spatial resolution.

To overcome this limitation and to speed up dynamic data acquisition, a range of techniques has been proposed. Besides parallel imaging techniques (1–3), data sharing methods such as keyhole (4,5) and other view-sharing strategies (6–8) have been investigated. Keyhole and view-sharing methods modify the sampling distance along the temporal dimension for different *k*-space positions resulting in differences in temporal fidelity as a function of spatial harmonics of the dynamic object. In many angiographic applications the loss of temporal fidelity in edge information from view-sharing has been found negligible given appropriate undersampling schedules (9). More advanced techniques such as "unaliasing by Fourier-encoding the overlaps using the temporal dimension" (UNFOLD) (10) or Noquist (11) exploit the fact that usually only a fraction of the field-of-view (FOV) requires the full temporal bandwidth. This allows for more efficient packing of signals in the spatiotemporal frequency domain (12). As these techniques achieve gains in acquisition speed by skipping phase-encode steps and subsequent recovery of missing information based on difference in dynamics across the FOV, they are often referred to as reduced FOV methods.

To guide image reconstruction in an adaptive rather than static manner, prior information about the dynamics of the object may be measured directly. In *k-t* broad-use linear acquisition speed-up technique (*k-t* BLAST) (13), a low resolution scan acquired at the full temporal bandwidth is performed either before (in the case of periodic motion) or interleaved with the actual data acquisition. These "training" data have been demonstrated to allow resolving aliasing from undersampling along the spatial and temporal dimensions very efficiently. Since the information about the object is actually measured rather than simply assumed as in the view-sharing approach, this method can also be successfully applied in cases with complex dynamic motion such as in cardiac imaging or in flow imaging (14,15). The only prerequisites for the *k-t* BLAST reconstruction are spatiotemporal correlations to be present in the data, and these correlations to be accurately captured by the training scan.

In general, correlation or redundancy in the data infers that the data is compressible, i.e., the data can be represented by fewer coefficients in a certain basis. Dynamic data can undergo substantial compression as demonstrated by modern algorithms like MPEG-4 (Moving Pictures Expert Group; MPEG-4; ISO/IEC 14496-5:2001), which can achieve high compression rates without or with very little loss in image quality. Compression in the conventional sense is unfortunately not directly applicable to MRI since the object is typically not known beforehand and also the data may possibly not be acquired in the corresponding basis given the encoding mechanism used in MRI. Nevertheless, it raises the question of whether general frameworks for exploiting data redundancy can be adapted under certain circumstances.

A first step toward this direction was made by David Donoho et al. (16), who have set the basis by defining the discrete uncertainty principle, the discrete analogon of the Heisenberg uncertainty principle. More recent publications (17,18) outline a general mathematical framework for the reconstruction of compressible signals from undersampled data, a method referred to as compressed sensing (CS) hereafter. The work gives guidance as to how a compressible signal (i.e. a signal that is sparse in any known basis) has to be acquired and reconstructed. Furthermore a sampling criterion for such signals is derived, comparable to the Nyquist theorem.

Institute for Biomedical Engineering, University of Zurich and Swiss Federal Institute of Technology, Zurich, Switzerland.

Grant sponsor: SEP Life Sciences of ETH Zurich; Grant number: TH7/02-2, Grant sponsor: Swiss Commission for Technology and Innovation; Grant number: 8005.3 LSPP-LS; Grant sponsor: Philips Medical Systems.

*Correspondence to: Sebastian Kozerke, PhD, Institute for Biomedical Engineering, University and ETH Zurich, Gloriastrasse 35, 8092 Zurich, Switzerland. E-mail: kozerke@biomed.ee.ethz.ch

Received 21 April 2007; revised 27 September 2007; accepted 15 October 2007.

DOI 10.1002/mrm.21477
Published online in Wiley InterScience (www.interscience.wiley.com).

Widespread application of these principles in MRI is handicapped by the fact that general anatomical MR images are not sparse in the image domain directly. One exception relates to angiography, in which image content is typically sparse. Initial work on applying CS on angiographic data has been published (17,19).

To apply CS to images, which are only sparse in a transform domain, such as the wavelet or the finite differences domain, some prior knowledge about the object is needed in order to choose the right sparsifying transformation, although the discrete cosine transform or the wavelet transform used for JPEG and the JPEG2000 compression (Joint Photographic Experts Group; JPEG; ISO/IEC IS 10918-1 | ITU-T) seem to be robust sparsifying transformations for many types of images.

In this work, CS is adapted to dynamic MRI. In two-dimensional (2D) dynamic imaging the data are acquired in the k_x-k_y-t space and the corresponding "image" domain is described by the x-y-f space, where f denotes temporal frequency. In most cases of dynamic imaging only parts of the FOV require the full temporal bandwidth, with some parts even being static and therefore exhibiting only signal at the temporal direct current (DC) frequency in the x-y-f space. The image domain of a dynamic dataset therefore intrinsically offers sparsity regardless of the underlying motion properties and no further sparsifying transformation is necessary. In the context of dynamic imaging, CS can be considered a reduced FOV method similar to previous methods in which the sparsity of the object in a suitable domain is exploited. The present study aims at assessing the potential of CS in dynamic MRI and compares the results obtained from computer simulations and decimation of fully-sampled in vivo cardiac data to the k-t BLAST method.

THEORY

CS describes in a very general manner how an unknown vector $\mathbf{x}$ of length m can be reconstructed from n ($n < m$) linear functionals. This is an underdetermined problem in linear algebra but under certain conditions the sparsity constraint on $\mathbf{x}$ allows for an exact solution as described (18). A special case for this linear functional is the Fourier transform and in this context CS describes how a sparse image of size m can be reconstructed from its n k-space samples when n is substantially smaller than m (i.e., the Nyquist criterion is violated). An extensive description and some examples of this special case of CS are given in Ref. 17 and only the main results are summarized in the following.

Let $f \in \mathbf{C}^N$ be a discrete complex signal with support T and its corresponding Fourier transform $\hat{f} \in \mathbf{C}^N$ with support S. (The support of f defines the set of arguments for which f takes nonzero values). The original signal f can be easily reconstructed if all the Fourier coefficients on S are known by setting the residual coefficients $\in$ S to zero and taking the inverse Fourier transform. Because in general f and therefore S are unknown beforehand, every coefficient needs to be sampled to avoid image artifacts. In case f is known to be sparse i.e., $|T| << N$, the Fourier transform $\hat{f}$ cannot be sparse too due to the uncertainty principle (16), inferring that $\hat{f}$ has a "broad" support S. The discrete uncertainty principle therefore gives a lower bound for the sum of the support sizes in a discrete Fourier domain pair similar to the continuous case, but on the other hand also offers some surprising properties that have been discussed (16). The most striking property is the possibility to *exactly* recover a sparse signal from its incomplete frequency information.

A more detailed analysis (17) of these properties revealed that a sparse signal f can be recovered from an incomplete, randomly chosen subset $\Omega \subset S$ of frequencies by solving the convex optimization problem (20):

$$\min_g \sum_{t=1}^{N} \|g(t)\|, \text{ s.t. } \hat{g}(\omega) = \hat{f}(\omega) \text{ for all } \omega \in \Omega \qquad [1]$$

The solution g to this constrained optimization problem is unique and equal to the original signal f. This works for an overwhelming percentage of signals f as shown (17) if f is *sparse* and its Fourier coefficients are sampled *randomly*. One example, where this framework fails is the Dirac comb signal in combination with a sampling pattern that samples the zero signals in-between the signal peaks in the corresponding conjugate domain. The probability of "accidentally" choosing such a sampling pattern picking the zero values is smaller than 10^{-13} if a signal length of 100 is assumed. This demonstrates the robustness of the framework in medical imaging, in which the size of signals is typically much greater and the shape is considerably less regular than a Dirac comb. Since objects similarity across subjects is relatively high in a mathematical sense (e.g., the heart can always be decomposed into piecewise constant functions for a given error tolerance) the same random sampling scheme can be reused for different scans and different subjects. With respect to differences in noise level, reconstruction by convex optimization has proved to be robust to noise with high reproducibility (21).

The random data sampling can easily be achieved in dynamic MRI by randomly skipping phase encoding lines in each time-frame generating a random sampling pattern in the k_y-t space as shown in Fig. 1a. Such an undersampling scheme leads to an incoherent signal aliasing in the y-f space (Fig. 1b and c) unlike regular undersampling (Fig. 1d), which leads to distinct aliases as shown in Fig. 1e and f.

The other prerequisite, the sparseness in the image may be introduced using the Wavelet transform along the spatial dimension and a Fourier transform along the temporal dimension (22). Alternatively, a Fourier transform along the temporal dimension may be sufficient assuming that large parts of the FOV are not moving at all or only at low temporal frequencies. If the sparsity σ in the y-f space is quantified by the quotient of the signal size and its support size, then the example signal in Fig. 2c has a sparsity of 4.7.

Minimizing the ℓ_1 norm of a function under constraints as given in Eq. [1] is a convex optimization problem that can robustly be solved using interior point methods (23) at the expense of some computational effort. For the example given in Fig. 2 the memory requirements are already in the order of several Gigabytes with standard solvers and the

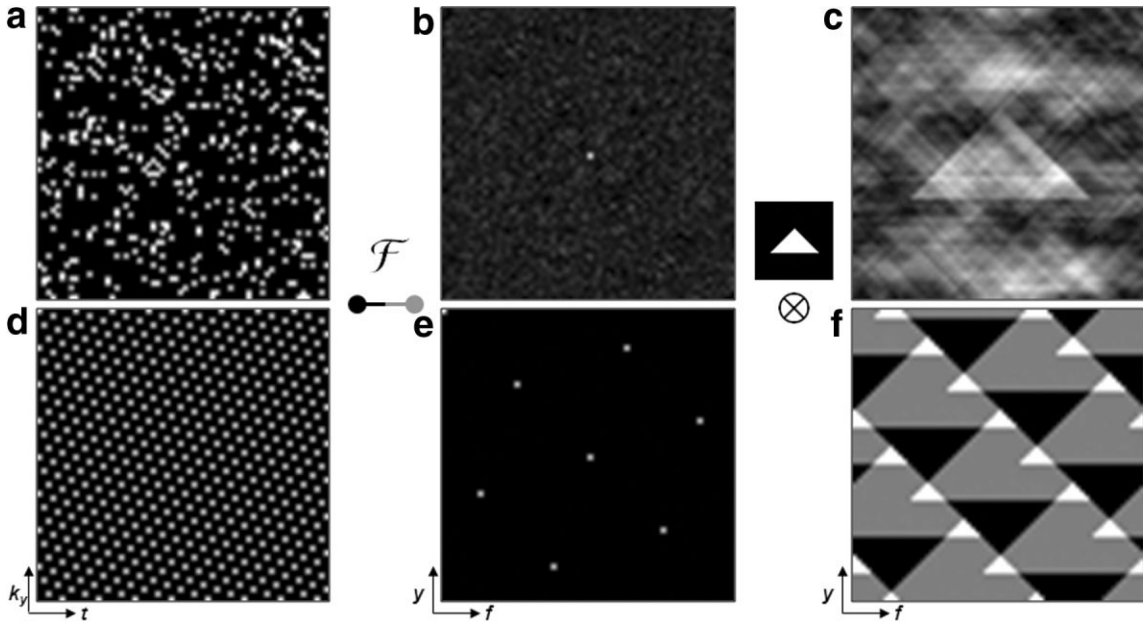

FIG. 1. Random (**a**) and regular (**d**) sampling patterns with corresponding point spread functions (**b**,**e**). The convolution with a triangular shaped object shows the different aliasing patterns (**c**,**f**). The aliasing generated by the random sampling patterns still allows distinguishing between the true object and its aliases, an important observation underlying the CS framework.

computing time is in the order of tens of hours. However, this constrained ℓ_1 minimization is only one possibility to find or approximate the sparsest solution of the underdetermined linear system which is in general a non-deterministic polynomial time (NP) hard problem. To solve this problem, other algorithms have been proposed such as projection onto convex sets (24) with modifications (25). "Practical signal recovery from random projections"; (2005, Manuscript, available on-line) or orthogonal matching pursuit (OMP) approaches (26,27). D. Donoho, Y. Tsaig, I. Drori, JL Starck, "Sparse solution of underdetermined linear equations by stagewise orthogonal matching pursuit"; (unpublished results). Many of these algorithms offer less theoretical mathematical strictness than the ℓ_1 minimization, but on the other hand require less computing resources, yielding the same reconstruction performance and are therefore more favorable for practical use.

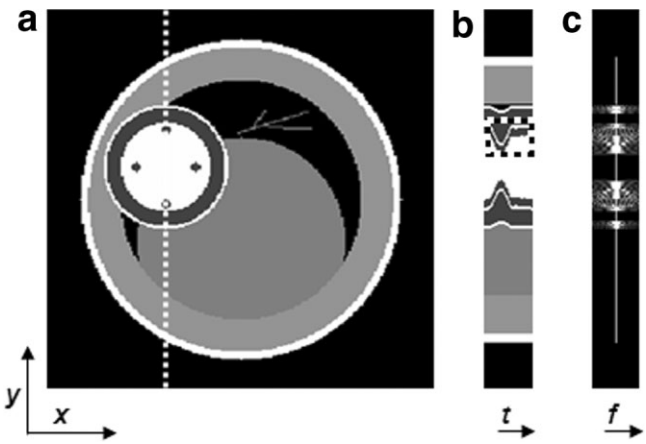

FIG. 2. The simulation model is shown in (**a**) with the corresponding y-t space along the dotted line in (**b**). The ROI used for the error calculations is indicated by the dotted line. The Fourier transform along t yields the corresponding sparse representation in y-f space shown in (**c**).

METHODS

Random Sampling

The mathematical framework in CS is based on truly random sampling as it generates incoherent aliasing with high probability. In a practical setting, it may nevertheless be possible to constrain the random sampling to some extent while maintaining incoherent aliasing. To this end, a constraint random sampling pattern in *k-t* space can be generated taking into account following rationales: 1) the local temporal density of the sampling points should not vary too much e.g., if the data are collected in heart phases then every heart phase should have the same number of sampling points to achieve a maximum sampling efficiency; 2) because the sparse domain (x-f space) is not only sparse but also compact in most practical cases (Fig. 3c), the aliasing overlap in this domain can be further reduced by minimizing the distance between sampling points in the *k-t* space as it has been suggested for regular undersampling (28). To satisfy these two constraints, sampling patterns were generated from regular undersampling patterns as proposed in Ref. 28 by additionally shifting each sampling point randomly by –1, 0, or +1 position along the *k*-dimension. This ensures that every frame (heart phase) has the same number of sampling points and it also sets an upper limit to the maximal distance between sampling points. Such a constrained random sampling pattern is shown in Fig. 3b yielding a reduced aliasing pattern (Fig. 3e) for the exemplary x-f space compared to the unconstrained random sampling (Fig. 3d).

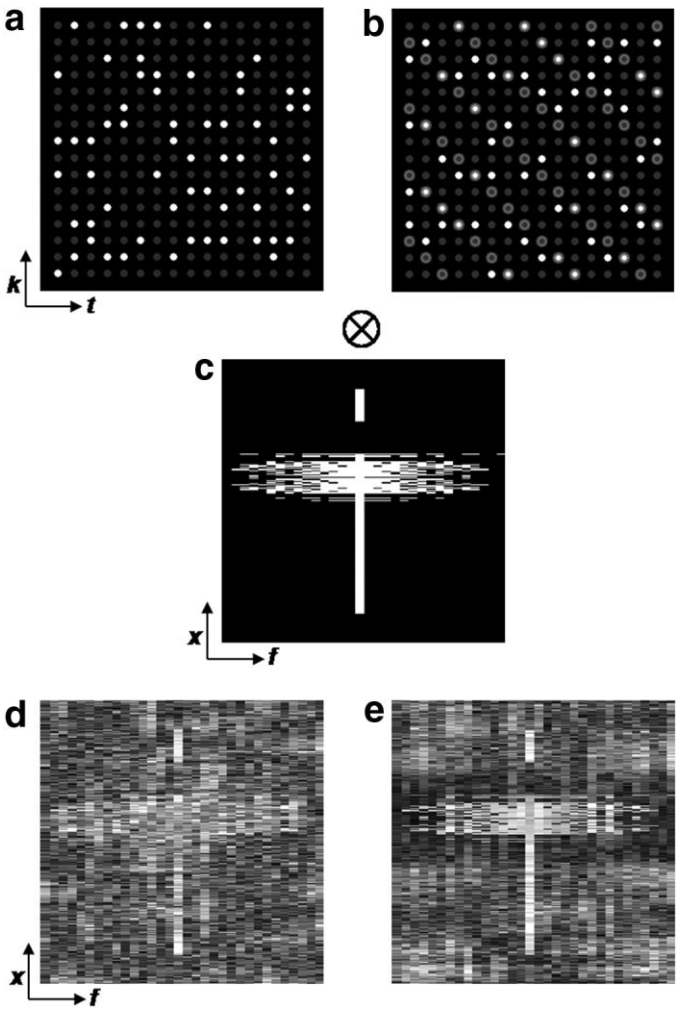

FIG. 3. Comparison of a random sampling pattern (**a**) with a constrained random sampling pattern (**b**), where sampling points on a regular sheared grid are randomly shifted along the *k*-dimension by –1, 0 or +1. The convolution with an exemplary x-f space (**c**) yields the corresponding aliased x-f spaces in (**d**,**e**), demonstrating decreased aliasing overlap in the constrained random sampling case (e).

Reconstruction and Quantification

To reconstruct the sparse solution in the x-f space a simple implementation of an OMP algorithm as described in (Ref. 27) was used. The algorithm starts from the aliased x-f space A_0 (the two-dimensional Fourier transform of the zero-filled sampling points), picks the pixel with the highest signal intensity and adds it to the final x-f space *I*. The aliasing *F* of this x-f space is calculated by convolution with the given point spread function and subtracted from the previous aliasing pattern. This iteration is performed until the maximum residual aliasing intensity in x-f space reaches the intensity of noise. In the case of noiseless simulation data the iteration is performed until this intensity is smaller than one millionth of the maximum signal in x-f space. This threshold mainly affects the runtime and not the quality of the reconstruction due to the greedy behavior of the iteration where signals with low energy levels are reconstructed last. After a first reconstruction run, a density map of nonzero pixels in the obtained final x-f space *I* is calculated to identify static areas in the image which have significantly lower density at non-dc frequencies relative to dynamic areas. The same reconstruction procedure is then repeated including this additional information by penalizing these areas in x-f space during the iteration process which further improves the result. This modification will be termed CS + penalty hereafter. The outline of the algorithm as described is given in Fig. 4.

To quantify the reconstruction error for the different reconstruction methods, the root-mean-square (RMS) error per pixel was calculated in a region of interest:

$$(E_{RMS,t})^2 = \frac{\sum_{i=1}^{N} |r_{i,t} - o_{i,t}|^2}{\sum_{i=1}^{N} |o_{i,t}|^2} \quad [2]$$

where $E_{RMS,t}$ denotes the relative RMS error at time frame t; $r_{i,t}$, and $o_{i,t}$ denote the ith pixel value at time frame t in the reconstructed and the original images, respectively, and N is the total number of pixels in the ROI considered. The total error E_{RMS} is calculated by additionally summing over the temporal dimension:

$$(E_{RMS})^2 = \frac{\sum_{t=1}^{T}\sum_{i=1}^{N} |r_{i,t} - o_{i,t}|^2}{\sum_{t=1}^{T}\sum_{i=1}^{N} |o_{i,t}|^2} \quad [3]$$

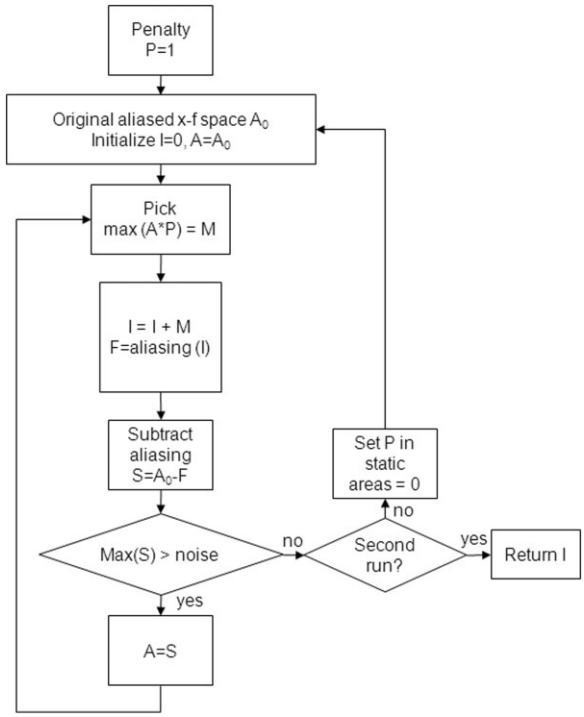

FIG. 4. Flowchart describing the implementation of the OMP reconstruction used in this work. See Reconstruction and Quantification section for a detailed description.

The specific choice of the ROI influences the magnitude of the RMS error and therefore different ROIs were used. Furthermore reconstructed images are included for visual comparison to reveal reconstruction characteristics.

Computer Simulation

For simulation purposes, a computer model implemented in MATLAB (The MathWorks, Natick, MA, USA) mimicking the heart in a short-axis view was used. The temporal signal evolution along the vertical profile indicated in Fig. 2a was evaluated. The corresponding acquisition *k*-space (*k-t* space) was obtained by data decimation. For *k-t* BLAST, two-, four-, and eight-fold undersampling was simulated with 11 central and fully-sampled profiles used for training, resulting in net acceleration factors of 1.9, 3.5, and 6.2, respectively. For random undersampling the data dimensions do not need to be an integer multiple of the reduction factor and therefore reduction factors from 2 to 6.5 could be covered at a finer step size of 0.3. E_{RMS} of the ROIs indicated in Fig. 2b was calculated to compare the reconstructions for the different datasets and reduction factors. To investigate the impact of noise on the reconstructions, Gaussian noise was added to the noiseless model dataset (Fig. 2b), yielding different signal-to-noise ratios (SNRs) on the myocardium (dark structure in the ROI). Furthermore, the artifact characteristics were investigated by comparing reconstructed images with a similar RMS error for both methods. The influence of sparsity was studied by comparing the reconstruction errors in case of a myocardial SNR of 15 for the small and the large heart model with sparsities σ of 7.5 and 4.7, respectively. The same noise level was also used for the dataset that compares the RMS error of the proposed constrained random sampling pattern to the unconstrained, completely random sampling pattern.

Dynamic Cardiac Imaging

A short-axis cine dataset was acquired on a Philips 3.0T Achieva system (Philips Medical Systems, Best, The Netherlands) using an eight-element coil array. An ECG-triggered balanced steady-state free precession (SSFP) sequence with a TR of 3.8 ms was used. The image resolution was $1.7 \times 1.7 \times 8$ mm^3 and 24 heart phases were acquired in one breathhold of ~18 s. A profile intersecting the papillary muscles was reconstructed for different reduction factors with both *k-t* BLAST and CS. Furthermore, the x-f spaces of this profile were calculated to reveal differences of the reconstructions in the spatiotemporal domain. For full image reconstruction, the dataset was decimated regularly with a *k-t* factor of 4 and 21 training profiles, yielding a net speedup factor of 3, and randomly with an undersampling factor of 3. For visual comparison of the results from *k-t* BLAST and CS reconstruction, timeframes during rapid motion of the heart at the beginning of the cardiac cycle were selected. This first timeframe was chosen because the motion discontinuity between the beginning and the end of the acquired cycle arising from the temporal gap in prospective triggering results in significant signals at high temporal frequencies in x-f space, which are difficult to treat with both reconstruction methods. To assess the reconstruction quality, $E_{RMS,t}$ was calculated for a ROI around the heart.

Fourier Velocity-Encoded Imaging

The higher dimensionality of a Fourier velocity-encoded (FVE) (29,30) dataset is expected to increase the sparsity of the data and therefore should allow for higher reduction factors. This was tested on data from a healthy volunteer, in whom the pulsatile flow in the carotid artery was examined. The scan parameters were: image resolution = $1.2 \times 1.2 \times 10$ mm^3, TE/TR = 5.7 ms/12.0 ms, and 16 FVE steps with maximum velocity encoding v_{enc} = 100 cm/s. The size of the acquisition matrix was 128×116, 32 cardiac triggered timeframes were acquired on a Philips 1.5T Intera whole-body system using a dedicated carotid coil element. The total scan time was 16 min. A profile that passes through the center of the carotid artery was chosen for further investigations. The dataset (k_x-k_v-*t* space) was undersampled by a *k-t* factor of 8, using nine training profiles in both the phase-encoding and velocity-encoding directions (31), resulting in a net acceleration factor of 6.8. The sparse domain used for the CS reconstruction is the three-dimensional Fourier transform of the data, the x-v-f space.

The peak flow and velocity spectra for different voxels were compared. The velocity data were zero-filled prior to Fourier transform.

RESULTS

Simulations

Figure 5a shows the reconstruction errors in the ROI indicated in Fig. 5d for different undersampling factors for the

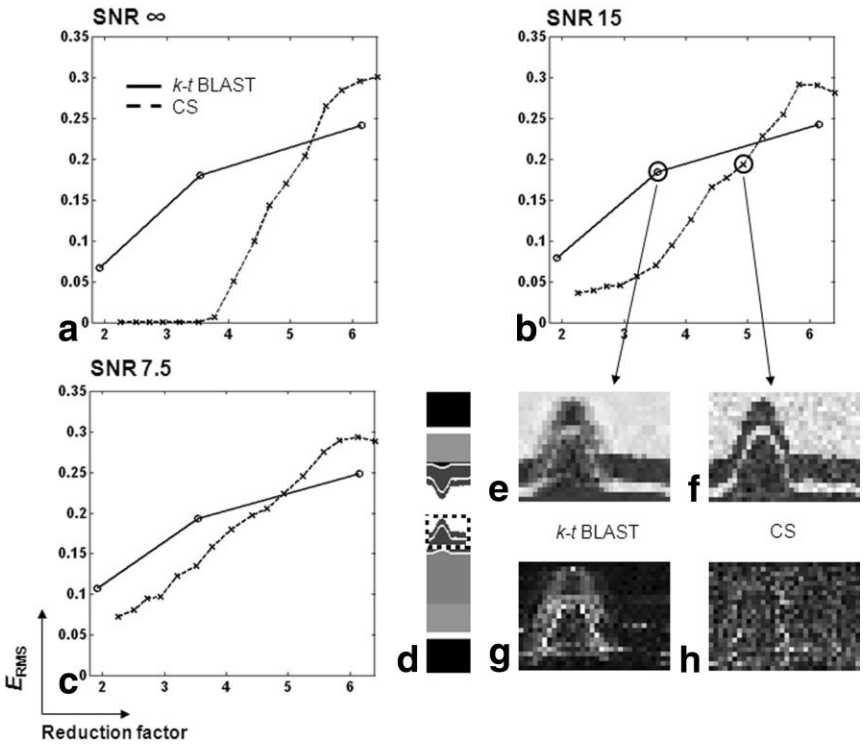

FIG. 5. Total RMS error in the ROI indicated in (**d**) for different reduction factors and noise levels (**a**–**c**). Results for the different reconstruction methods yielding similar RMS error are shown in (**e**–**h**) for visual comparison.

CS reconstruction (dotted line) and compares them to a *k-t* BLAST reconstruction (solid line). The impact of different noise amplitudes is depicted in Fig. 5b and c, resulting in a lower E_{RMS} for the CS reconstruction for reduction factors <5. The different error characteristic of the two methods is visualized in Fig. 5e–h (SNR of 15 on the myocardium). The corresponding E_{RMS} in the ROI was 0.19 and 0.18 for the CS and the *k-t* BLAST reconstruction, respectively. However, the error distribution in the CS reconstruction appears to be more uniform. The influence of sparsity, which was assessed using heart models of different sizes as shown in Fig. 6a, proved to be more pronounced for the CS reconstruction than for *k-t* BLAST. In general, the CS reconstruction error can be significantly reduced using the proposed constrained random sampling scheme and the penalizing term as demonstrated in Fig. 6b.

Dynamic Cardiac Imaging

The reconstruction results of heart phase 1 and 4 corresponding to time points at the beginning of systole and at peak systole for the in vivo dataset are shown in Fig. 7c. The corresponding difference images are scaled by a factor of 10 to reveal details. From the difference maps it is seen that CS results in a more homogenous error distribution across the FOV while errors in *k-t* BLAST occur mainly at edges of dynamic structures. Also along the time axis the

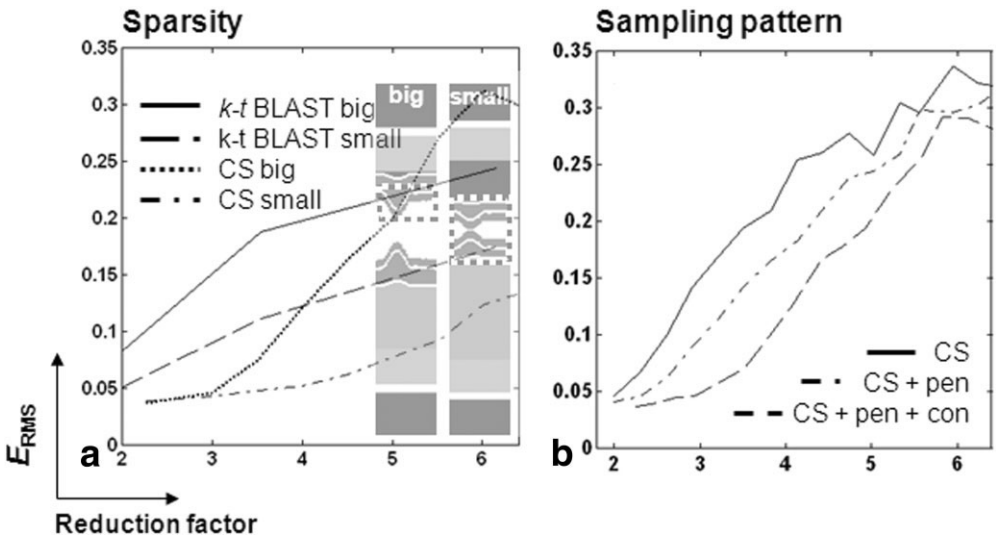

FIG. 6. To demonstrate the influence of sparsity, the reconstruction error for the big model heart is compared to a small heart in (**a**), which features an increased sparsity of 7.5 in x-f space. The dotted areas indicate the ROIs for the computation of the RMS errors. The influence of the constrained random sampling pattern and the penalizing term on the reconstruction quality is shown in (**b**). The OMP reconstruction with random sampling without the penalizing term is labeled CS, with the penalizing term CS + pen. The constrained random sampling is labeled CS + pen + con.

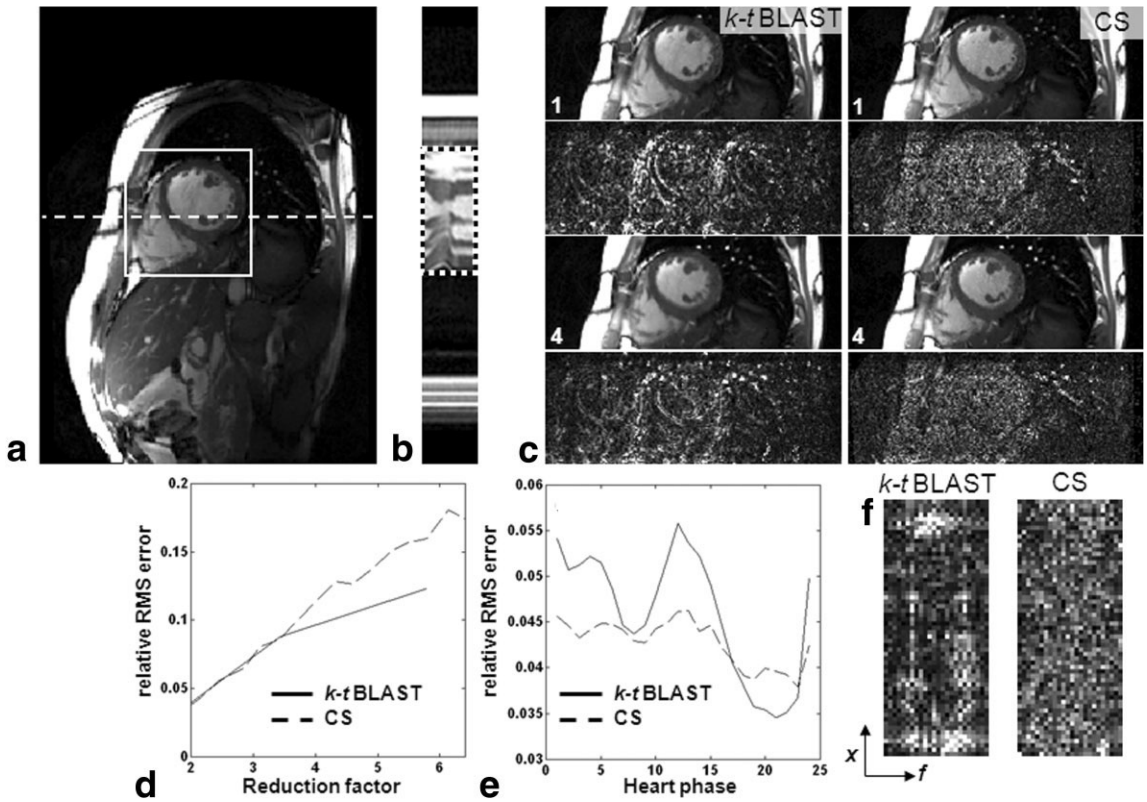

FIG. 7. Results from *k-t* BLAST and CS based on decimated in vivo data from a fully-sampled short-axis cine acquisition of the heart. A profile along the dashed line intersecting the papillary muscles (**a**) is shown in (**b**). Heart phases 1 and 4 of the *k-t* BLAST and the CS reconstruction are shown in (**c**) along with the corresponding difference images (scaled by a factor of 10 to visualize details). RMS errors are plotted as functions of the reduction factor (**d**) and as functions of the heart phase (**e**) for the ROIs indicated in (b) and (a), respectively. Scaled difference images of the x-f spaces for the ROI indicated in (b) are shown in (f). It is seen that k-t BLAST results in inhomogeneous distribution of error in both the x-t and x-f plots with largest errors occurring at locations corresponding to dynamic object edges. In contrast, the error in CS is more homogeneously distributed and smaller for highly dynamic object features.

CS reconstruction error is distributed more uniformly as shown in Fig. 7e, depicting $E_{RMS,t}$ for the ROI indicated in Fig. 7a as a function of heart phase. This behavior is also reflected in the difference images of the reconstructed x-f spaces shown in Fig. 7f. The RMS error for a profile intersecting the papillary muscles (Fig. 7b) shown in Fig. 7d was similar for both methods at the chosen reduction factor of 3.

FVE Imaging

The carotid artery indicated with a circle is shown in Fig. 8a along with a velocity profile taken along the dotted line. The peak flow velocities along this profile are shown in Fig. 8b for the original dataset as well as for the undersampled data, revealing underestimation of peak maximum and minimum flow in the *k-t* BLAST reconstruction, which is less pronounced in the CS images. A more detailed analysis in Fig. 8c and d shows the velocity distribution of two different voxels. Figure 8c displays a spectrum of the central pixel in the carotid artery during the upslope at 154 ms of the systolic flow pulse. The spectrum for a pixel at the border of the carotid artery with two distinct velocity peaks is shown in Fig. 8d. All spectra are normalized to their corresponding maximum values.

DISCUSSION AND CONCLUSION

In this work CS was adapted to dynamic MRI and compared to *k-t* BLAST imaging using a computer model, fully sampled cardiac, and FVE in vivo data that were decimated to simulate accelerated data acquisition. The introduction of constrained random sampling as well as incorporation of a penalty procedure applied during a second run of the iterative reconstruction algorithm have been demonstrated to improve CS reconstruction of the example data sets significantly.

In the case of noiseless data, CS was demonstrated to perfectly recover the image of the cardiac model up to an undersampling factor of about three. Beyond that factor, the reconstruction error increased. Accordingly, two regimes can be distinguished: a lower regime, in which the reconstruction is exact and does not depend on the undersampling factor and an upper regime, where E_{RMS} grows proportional with the amount of undersampling. The critical reduction factor at which this "phase transition" occurs depends mainly on the sparsity σ of the data. This transition was found to occur at an undersampling factor around $\frac{\sigma}{1.5}$ (Figs. 5a and 6a). Other publications (17,25,27) (D. Donoho, Y. Tsaig, I. Drori, JL Stark. ″Sparse solution of

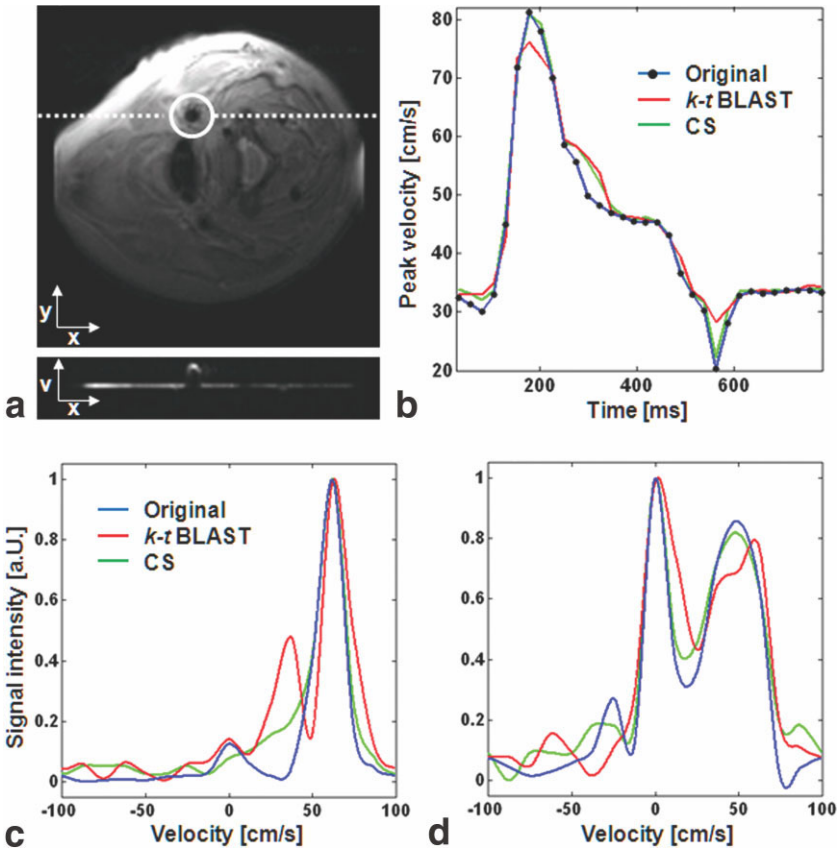

FIG. 8. Fourier velocity-encoded data. **a:** The carotid artery (white circle) is shown, along with a corresponding velocity profile taken at the dotted line indicated. **b:** The peak velocities for the original and the undersampled datasets are given. Velocity spectra are shown for a central pixel of the carotid artery (**c**) and for a pixel at the vessel border (**d**).

underdetermined linear equations by stagewise orthogonal matching pursuit", unpublished results) indicated lower values for this transition ranging from $\frac{\sigma}{5}$ to $\frac{\sigma}{2}$. This is due to the constrained (not *completely*) random sampling pattern used here, which maximizes the aliasing distance. For a completely random sampling pattern the phase transition occurs at lower reduction factors as shown in Fig. 6b and is therefore in good agreement with the aforementioned findings.

If Gaussian noise is added to the data, the x-f space is not strictly sparse anymore but the signal is still compressible and therefore the CS framework can still be applied. Nevertheless, the E_{RMS} of the CS reconstruction is significantly increased and the phase transition is no longer as evident as before. The major part of E_{RMS} increase is due to the SNR decrease, which is proportional to the square root of the undersampling factor. Additionally, E_{RMS} is increased, because signal components below the noise level in x-f space are not recovered by the algorithm.

On the other hand, the RMS error of the *k-t* BLAST reconstruction mainly depends on the quality of the training data, which is less affected by noise due to its low spatial resolution and therefore the error of the *k-t* BLAST reconstruction is less increased.

From these simulations some premises for a successful application of CS in dynamic MRI can be derived: 1) first, the data has to have sufficient SNR. For example, at fourfold acceleration the SNR is reduced at least two-fold with corresponding noise amplification in the CS reconstruction. The *k-t* BLAST reconstruction tends to smooth signals out, or, equivalently, it sets signals at high temporal frequencies to background. This compensates for the SNR decrease to some extent. According to the Rose model (32,33) the SNR in an image should not drop below three to five otherwise structures cannot be distinguished from noise anymore and therefore the subjective image quality for the CS reconstruction may become worse than that for the *k-t* BLAST reconstruction; 2) second, the data needs to be highly compressible to expand the regime below the critical reduction factor as much as possible to achieve high reduction factors without introducing additional errors. In the approach presented here, the compressibility depends on the ratio between static and moving tissue along the undersampled dimensions. To this end, encoding higher dimensional spaces is preferred. For instance, the sparsity of the computer model shown in Fig. 2a in the 2D x-f space (Fig. 2d) is 4.7, but the full 3D x-y-f space would have a sparsity of 16. Since random Cartesian sampling along the readout direction is not practical in MRI, radials or randomly perturbed spirals (34) are needed to exploit both spatial dimensions in dynamic 2D MRI. In a logical extension, dynamic 3D MRI would therefore offer both SNR and sparsity advantages. Instead of encoding more spatial dimensions, functional encoding dimensions may be used to increase the sparsity as demonstrated with FVE imaging. In typical applications, large sparsity values may be achieved since the dynamic object of interest (the vessel) is usually small compared to the surrounding tissue.

In the idealized simulation settings only relatively low sparsity in x-f space was obtained. In vivo data provided

even less sparsity due to additionally moving structures like blood vessels or due to ghosting artifacts that are reflected in a higher CS reconstruction error for the in vivo dataset (Fig. 6d) compared to the model heart (Fig. 5a). Therefore, only a relatively small reduction factor of 3 was chosen for the in vivo dataset. As in the simulations, a comparison of $E_{RMS,t}$ shows that the CS reconstruction has a more uniform error distribution in space and time. The reconstruction error of the *k-t* BLAST method is largest at tissue borders and/or at timeframes in which motion occurs. This is mainly due to partial volume effects in the training data. Heart phases during diastole therefore exhibit a smaller $E_{RMS,t}$ for the *k-t* BLAST reconstruction because the additional noise stemming from the undersampling is partly removed by the *k-t* BLAST filter.

For the FVE dataset, a higher reduction factor of 6.8 was possible due to the increased sparsity in x-v-f space. The peak flow values and the velocity spectra showed improved fidelity for the CS method as compared to *k-t* BLAST.

In summary, CS offers a promising framework for scan-time reduction in dynamic MRI if sufficient base SNR is given and provided that data is sparse enough. The Fourier transform along the temporal dimension offers a straightforward way of sparsifying dynamic data and simplifies the reconstruction algorithm because no further sparsifying transform such as the Wavelet transform is needed. CS reconstruction artifacts feature noiselike properties with a uniform distribution over the FOV, which might be less disturbing to the observer's eye than blurring or distinct ghosting. Especially in cases with small moving structures that are insufficiently resolved by the *k-t* BLAST training data, the CS framework might prove a useful alternative.

ACKNOWLEDGMENTS

We thank Christof Baltes and Michael Schacht Hansen for providing the Fourier velocity data and the corresponding analysis tools.

REFERENCES

1. Sodickson DK, Manning WJ. Simultaneous acquisition of spatial harmonics (SMASH): fast imaging with radiofrequency coil arrays. Magn Reson Med 1997;38:591–603.
2. Pruessmann KP, Weiger M, Scheidegger MB, Boesiger P. SENSE: sensitivity encoding for fast MRI. Magn Reson Med 1999;42:952–962.
3. Griswold MA, Jakob PM, Heidemann RM, Nittka M, Jellus V, Wang J, Kiefer B, Haase A. Generalized autocalibrating partially parallel acquisitions (GRAPPA). Magn Reson Med 2002;47:1202–1210.
4. van Vaals J, Brummer M, Dixon W, Tuithof H, Engels H, Nelson R, Gerety B, Chezmar J, den Boer J. "Keyhole" method for accelerating imaging of contrast agent uptake. Magn Reson Med 1993;3:671–675.
5. Jones R, Haraldseth O, Muller T, Rinck P, Oksendal A. k-Space substitution: a novel dynamic imaging technique. Magn Reson Med 1993;29:830–834.
6. Parrish T, Hu X. Continuous update with random encoding (CURE): a new strategy for dynamic imaging. Magn Reson Med 1995;33:326–336.
7. Doyle M, Walsh E, Blackwell G, Pohost G. Block regional interpolation scheme for k-space (BRISK): a rapid cardiac imaging technique. Magn Reson Med 1995;33:163–170.
8. Zaitsev M, Zilles K, Shah N. Shared k-space echo planar imaging with keyhole. Magn Reson Med 2001;45:109–117.
9. Korosec FR, Frayne R, Grist TM, Mistretta CA. Time-resolved contrast-enhanced 3D MR angiography. Magn Reson Med 1996;36:345–351.
10. Madore B, Glover GH, Pelc NJ. Unaliasing by Fourier-encoding the overlaps using the temporal dimension (UNFOLD), applied to cardiac imaging and fMRI. Magn Reson Med 1999;42:813–828.
11. Brummer ME, Moratal-Perez D, Hong CY, Pettigrew RI, Millet-Roig J, Dixon WT. Noquist: reduced field-of-view imaging by direct Fourier inversion. Magn Reson Med 2004;51:331–342.
12. Tsao J. On the UNFOLD method. Magn Reson Med 2002;47:202–207.
13. Tsao J, Boesiger P, Pruessmann KP. k-t BLAST and k-t SENSE: dynamic MRI with high frame rate exploiting spatiotemporal correlations. Magn Reson Med 2003;50:1031–1042.
14. Hansen M, Baltes C, Tsao J, Kozerke S, Pruessmann K, Boesiger P, Pedersen E. Accelerated dynamic Fourier velocity encoding by exploiting velocity-spatio-temporal correlations. MAGMA 2004;17:86–94.
15. Baltes C, Kozerke S, Hansen M, Pruessmann K, Tsao J, Boesiger P. Accelerating cine phase-contrast flow measurements using k-t BLAST and k-t SENSE. Magn Reson Med 2005;54:1430–1438.
16. Donoho D, Stark P. Uncertainty principles and signal recovery. Siam J Appl Math 1989;49:906–931.
17. Candes E, Romberg J, Tao T. Robust uncertainty principles: exact signal reconstruction from highly incomplete frequency information. IEEE Trans Inf Theory 2006;52:489–509.
18. Donoho D. Compressed sensing. IEEE Trans Inf Theory 2006;52:1289–1306.
19. Lustig M, Donoho D, Pauly J. Rapid MR angiography with randomly under-sampled 3DFT trajectories and non-linear reconstruction. Society for Cardiovascular Magnetic Resonance Proceedings of the 9th Annual Meeting of the Society for Cardiovascular Magnetic Resonance (SCMR), Miami, FL, USA, 2006 (Abstract 326).
20. Nocedal J, Wright S. Numerical optimization. New York: Springer; 1999.
21. Candes E, Romberg J, Tao T. Stable signal recovery from incomplete and inaccurate measurements. Comm Pure Appl Math 2006;59:1207-1223.
22. Lustig M, Santos J, Donoho D, Pauly J. k-t SPARSE: High frame rate dynamic MRI exploiting spatio-temporal sparsity. In: Proceedings of the 14th Annual Meeting of ISMRM, Seattle, WA, USA, 2006 (Abstract 2420).
23. Chen S, Donoho D, Saunders M. Atomic decomposition by basis pursuit. Siam J Sci Comp 1999;20:33–61.
24. Bregman L. The method of successive projection for finding a common point of convex sets. Soviet Math Dokl 1965;6:688–692.
26. Gilbert A, Guha S, Indyk P, Muthukrishnan S, Strauss M. Near-optimal sparse Fourier representations via sampling. In: Proc 34th ACM Symposium on Theory of Computing, Madrid, 2002:152–161.
27. Tropp J, Gilbert A. Signal recovery from random measurements via orthogonal matching pursuit. IEEE Trans Info Theory; in press.
28. Tsao J, Kozerke S, Boesiger P, Pruessmann K. Optimizing spatiotemporal sampling for k-t BLAST and k-t SENSE: application to high-resolution real-time cardiac steady-state free precession. Magn Reson Med 2005;53:1372–1382.
29. Moran P. A flow velocity zeugmatographic interlace for NMR imaging in humans. Magn Reson Imaging 1982;1:197–203.
30. Redpath T, Norris D, Jones R, Hutchison J. A new method of NMR flow imaging. Phys Med Biol 1984;29:891–895.
31. Hansen MS, Kozerke S, Pruessmann KP, Boesiger P, Pedersen EM, Tsao J. On the influence of training data quality in k-t BLAST reconstruction. Magn Reson Med 2004;52:1175–1183.
32. Haacke E, Brown R, Thompson M, Venkatesan R. Magnetic resonance imaging—physical principles and sequence design. New York: John Wiley & Sons; 1999.
33. Rose A. Vision: human and electronic. In: Optical physics and engineering. New York: Plenum; 1973, pp. 25.
34. Lustig M, Lee J, Donoho D, Pauly J. Faster imaging with randomly perturbed, undersampled spirals and L1 reconstruction. In: Proceedings of the 13th Annual Meeting of ISMRM, Miami Beach, FL, USA, 2005 (Abstract 685).